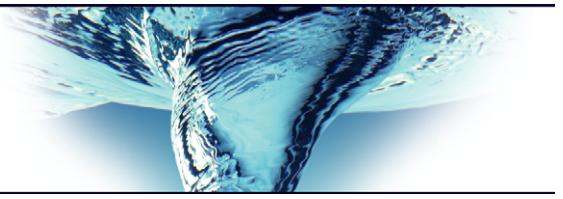
J. Fluid Mech. (2013), *vol.* 733, R4, doi:10.1017/jfm.2013.470



JFM RAPIDS
journals.cambridge.org/rapids

Levitation of a drop over a moving surface

Henri Lhuissier[1],†, Yoshiyuki Tagawa[1,2],†, Tuan Tran[1] and Chao Sun[1],†

[1]Physics of Fluids Group, Faculty of Science and Technology, J.M. Burgers Center for Fluid Dynamics, University of Twente, PO Box 217, 7500 AE Enschede, The Netherlands

[2]Department of Mechanical Systems Engineering, Tokyo University of Agriculture and Technology, 2-24-16 Nakacho, Koganei-city, Tokyo, Japan

(Received 6 June 2013; revised 29 August 2013; accepted 4 September 2013;
first published online 25 September 2013)

We investigate the levitation of a drop gently deposited onto the inner wall of a rotating hollow cylinder. For a sufficiently large velocity of the wall, the drop steadily levitates over a thin air film and reaches a stable angular position in the cylinder, where the drag and lift balance the weight of the drop. Interferometric measurements yield the three-dimensional (3D) air film thickness under the drop and reveal the asymmetry of the profile along the direction of the wall motion. A two-dimensional (2D) model is presented which explains the levitation mechanism, captures the main characteristics of the air film shape and predicts two asymptotic regimes for the film thickness h_0: for large drops $h_0 \sim Ca^{2/3}\kappa_b^{-1}$, as in the Bretherton problem, where Ca is the capillary number based on the air viscosity and κ_b is the curvature at the bottom of the drop; for small drops $h_0 \sim Ca^{4/5}(a\kappa_b)^{4/5}\kappa_b^{-1}$, where a is the capillary length.

Key words: drops, lubrication theory, thin films

1. Introduction

A drop falling onto a solid or a liquid surface, such as a raindrop onto a wall or a puddle, is usually expected to make contact with the impacted surface. However, under certain conditions, the persistence of the air film separating the drop from the surface prevents contact. This counter-intuitive phenomenon has been investigated, both for its fundamental interest and for its importance in various applications, such as droplet combustion, separation of emulsions, and spray painting. Configurations promoting non-contact have been explored, e.g. encapsulating the drop with a hydrophobic powder (Aussillous & Quéré 2001), oscillating the liquid surface to periodically renew the air film (Couder *et al.* 2005), or heating the surface to maintain a vapour film

† Email addresses for correspondence: h.lhuissier@utwente.nl, tagawayo@cc.tuat.ac.jp, c.sun@utwente.nl

© Cambridge University Press 2013

https://doi.org/10.1017/jfm.2013.470 Published online by Cambridge University Press

(Quéré 2013) or to generate a Marangoni convection opposing the drainage of the air film (Dell'Aversana, Banavar & Koplik 1996).

We consider here a different situation where the levitation is maintained by moving a surface, which continuously entrains new air under the drop that balances the drainage of the film. This phenomenon has already been observed in a slightly different situation in which a drop levitates over a capillary hydraulic jump (Sreenivas, De & Arakeri 1999; Pirat *et al.* 2010; Duchesne *et al.* 2013). Sreenivas *et al.* (1999) suggested that the levitation is due to the pressure built-up generated by the lubrication flow under the drop. However, they did not observe or compute the pressure in the air film or its shape. Neitzel & Dell'Aversana (2002) considered a situation where the drop is not free to move: a drop is fixed on a solid plate and pressed against a moving solid surface. They measured the air film thickness and observed the asymmetric deformation of the drop. Later Smith & Neitzel (2006) also realized simulations of the flow using lubrication theory but did not give any prediction for the film thickness or air drag.

In order to shed light on the mechanism of levitation and study the details of the air film, we present here a simple experimental system allowing a steady levitation configuration in which the drop is free to move and deform. It is inspired by a similar configuration, used to investigate the motion of a bubble or a solid sphere in a rotating flow (Bluemink *et al.* 2005, 2008, 2009; Tagawa *et al.* 2013), and consists of a drop gently deposited onto the inner wall of a hollow solid cylinder rotating around its horizontal axis. For a sufficient rotation speed, the drop levitates and reaches a stable angular position, at which the drag and lift balance the drop weight. This stable levitation suggests that a steady flow settles around and underneath the drop. It allows us to measure the air drag on the drop and the three-dimensional (3D) shape of the air film where the lift force is generated.

We first introduce the setup and primary observations in § 2. Based on these observations, we present in § 3 a simplified two-dimensional (2D) model which accounts for the levitation of the drop and yields predictions for the air film thickness and the drag due to the air flow under the drop. The model is compared to our observations in § 4. Lastly the limits of the model and possible extensions are discussed in § 5.

2. Experimental setup and observations

2.1. *Experimental setup*

The experimental setup we used to study levitating drops is schematized in figure 1(*a*). It consists of a hollow glass cylinder, with length 500 mm and diameter 100 mm, rotated about its axis in the horizontal direction, with circumferential velocity V up to 3.0 m s^{-1}. Drops of silicone oil (viscosity $\nu = 50$ cSt, surface tension $\sigma = 20.8$ mN m^{-1}, and density $\rho = 961$ kg m^{-3}) with diameter between 1 and 3 mm are gently deposited on the inner surface of the rotating cylinder. When the wall velocity V is sufficiently large, the drop levitates and reaches a stable angular position α. The inner surface of the cylinder is generally covered with a thin layer of the same liquid as in the drop, with thickness less than 1.0 mm. This liquid layer, due to its smooth surface, significantly lengthens the levitating time. Nonetheless, it does not affect the levitation mechanism and the results presented below: for fixed wall velocity and drop size, we observed similar equilibrium angular position of the levitating drop, whether the cylinder surface is dry or wetted. For each experiment, the motion of the drop, its apparent diameter D and the angular position α (see figure 1) are measured

https://doi.org/10.1017/jfm.2013.470 Published online by Cambridge University Press

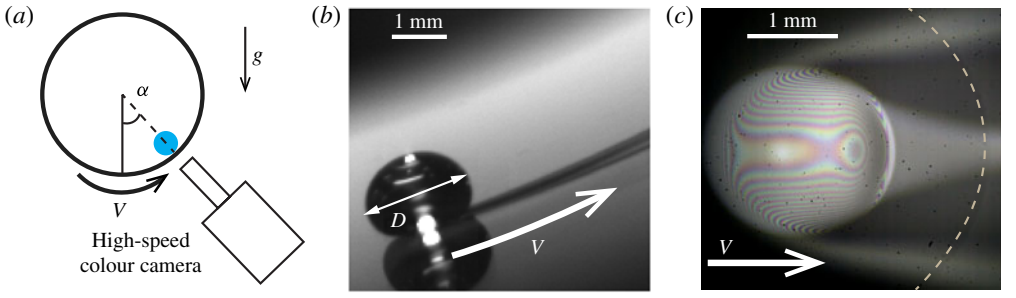


FIGURE 1. (*a*) Schematic (not to scale) of the experimental setup. (*b*) Side view of a levitating droplet. (*c*) Interferometric measurements of the air layer under the droplet.

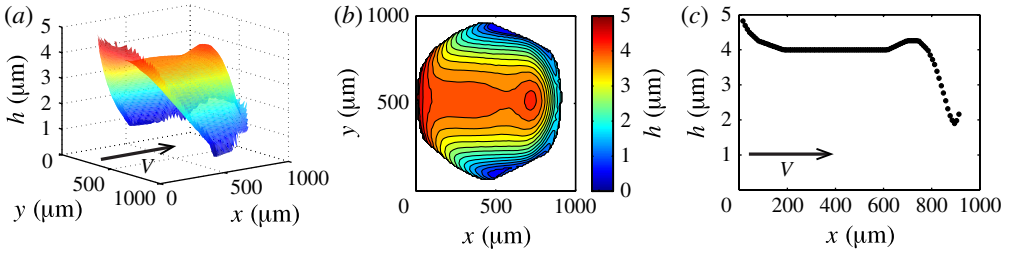


FIGURE 2. (*a*) 3D profile of the air film under the drop shown in figure 1(*c*). (*b*) Contour plot of the air film thickness profile. (*c*) Thickness along the plane of symmetry of the air film ($y = 500$ μm). The arrows in (*a,c*) indicate the direction of the wall motion.

on side-view recordings from a high-speed camera (SA1.1, Photron Inc.) which is aimed horizontally at the drop (not shown in figure 1*a*). A typical side-view of a drop levitating over a thin liquid layer is shown in figure 1(*b*).

The levitation of a drop indicates the existence of a thin air film underneath the drop. To measure the thickness of this air film, we use a colour interferometry method, which was described in detail by van der Veen *et al.* (2012), and successfully applied to measure the air layer thickness under droplets impacting on either solid or liquid surfaces (van der Veen *et al.* 2012; Tran *et al.* 2012, 2013). A colour high-speed camera (SA2, Photron Inc.) is connected to a long-working-distance microscope and is aimed perpendicularly at the cylinder wall, as shown in figure 1(*a*). As white light is supplied through a coaxial port of the microscope and is reflected both from the bottom surface of the drop and from the top surface of the liquid layer, a colourful interference pattern is formed and recorded. A typical image of this pattern is shown in figure 1(*c*). From a small strip across the fringes, we extract the absolute thickness of the air film (see van der Veen *et al.* 2012) and reconstruct the whole 3D air film profile by following the fringes with known thickness. In figure 2(*a,b*), we show the 3D profile and the contour plot extracted from the interference pattern shown in figure 1(*c*). The thickness profile in the plane of symmetry of the air film is shown in figure 2(*c*).

2.2. *Observations*

For each drop size D, levitation was only observed above a critical velocity. Below this velocity, the drop immediately touches the surface and is entrained by the moving

https://doi.org/10.1017/jfm.2013.470 Published online by Cambridge University Press

wall. Levitation is observed at lower velocity for small drops than for large ones. For a fixed drop size D, the equilibrium angular position α increases with V, illustrating that the ratio of the air drag to the drop weight increases.

The viscosity of the drop and liquid layer also influences the levitation. We observed that levitation is facilitated for viscosities around 50 cSt. For smaller viscosities, the drop may levitate for a short time but, due to the lower damping of capillary waves, the drop surface starts oscillating until it eventually touches the surface. For much larger viscosities, the drop does not levitate at all and makes contact immediately. This may be due to the fact that the relaxation time for the deformation of the drop becomes larger than the time for the drainage of the air film: the drop shape adapts too slowly to the flow below it to generate a sufficient lift before contact.

For $\nu = 50$ cSt (the only viscosity we will consider from now on), levitating drops appear stationary and α changes very little with time. More surprisingly, the liquid in the drop was found to be essentially motionless. By seeding the drop with particles (polyamid particles with a density of 1.03 g cm^{-3} and a diameter of 5 μm from Dantec), we could measure the velocity of the drop inner motion to be of the order of 1 mm s^{-1}, that is to say negligible with respect to the wall velocity $V \sim 1$ m s^{-1}. This suggests that the drop rotational motions do not contribute to the levitation mechanism, a conclusion we will use in § 3.

The interferometric measurements provide information on the shape of the air film underneath the drop. As figure 2 reveals, the bottom of the drop is essentially flat: the air film is typically a few micrometres thick and has an aspect ratio larger than 10^2. It consists of a flat portion, in the centre, which is surrounded, on three of its sides, by a ridge in the drop surface, corresponding to a smaller film thickness. This asymmetry of the air film shape along the direction of the wall motion is crucial for the generation of the lift. We will see in § 3 that the essential features of the 3D profiles can be captured by a simple 2D model.

We also observed that the extent of the flat region of the air film increases with the drop size. For drops larger than typically 10 mm, the drop shape is not stationary any more: it oscillates periodically until it eventually touches the surface. This suggests that an instability mechanism limits the size of the levitating drops to a value which is comparable with the capillary length.

3. Model

We now introduce a model for the levitating drop which both aims to clarify the mechanism of the levitation and to explain the typical thickness and shape of the air film separating the drop from the wall. We do not intend here to describe the details of the 3D shape of the air film, which would depend on every single experimental condition, as such an approach would not lend itself to any useful generalization. Instead, we rely on a simple 2D model that captures the essential features of the air film shape and allows analytical predictions in the limit of both large and small drops.

We consider a stationary liquid drop levitating above a flat solid wall moving at constant velocity $\boldsymbol{V} = V\boldsymbol{e_x}$, parallel to its surface. The weight of the drop is sustained by an air film which is dragged under the drop. The shape of the drop results from a balance between surface tension, gravity and viscous stresses in the air, respectively involving the surface tension σ of the liquid, gravity g and the density ρ of the liquid, and the dynamic viscosity $\eta = 1.81 \times 10^{-5}$ Pa s of the air. As already mentioned, we consider a 2D drop, that is to say a liquid mass having a cylindrical shape which is invariant along the direction tangent to the solid surface and perpendicular to $\boldsymbol{V}$. We

https://doi.org/10.1017/jfm.2013.470 Published online by Cambridge University Press

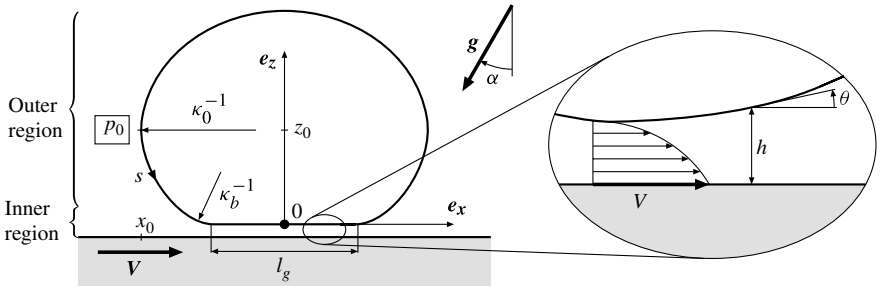


FIGURE 3. Schematic of the levitating drop.

assume that the liquid in the drop is at rest (as observed in § 2) and that inertial and compressibility effects in the air are negligible (the typical Reynolds number of the flow in the air film is 10^{-1}). In that case, the drop shape only depends on

$$Ca = \eta V/\sigma, \quad a\kappa_0 \quad \text{and} \quad \alpha, \tag{3.1}$$

which respectively stand for the capillary number, the product of the capillary length $a = \sqrt{\sigma/\rho g}$ with the curvature κ_0 of the drop at its widest point, and the angle between the direction normal to the wall and that of gravity (see figure 3). Considering the hydrostatic pressure field inside the drop, Laplace's equation relates the pressure p in the air, at the interface, with the coordinates $\{x, z\}$ and the curvature κ of the drop interface according to

$$\sigma(\kappa_0 - \kappa) + \rho g\,[(z_0 - z)\cos\alpha + (x_0 - x)\sin\alpha] = p - p_0, \tag{3.2}$$

where $\{x_0, z_0\}$ and p_0 respectively stand for the coordinates and the reference pressure at the widest point of the drop (see figure 3).

We first consider the limit of small capillary number, which corresponds to our experimental conditions where $Ca \sim 10^{-3}$, and seek asymptotic solutions. In that case, the influence of the viscous air flow on the drop shape is confined to the air film under the drop, as in the classical analysis by Landau & Levich (1942).

On the one hand, in the outer region, i.e. far from the air film (see figure 3), the profile of the drop is that of a sessile drop, that is to say prescribed by a balance between capillarity and gravity only. Letting $p = p_0$ in (3.2) yields, after integration, the coordinates x_S and z_S of the sessile drop interface

$$\frac{x_S}{a} = \int_\pi^\theta \frac{\cos\theta}{\sqrt{a^2\kappa_0^2 + 2\cos(\theta+\alpha)}}\,\mathrm{d}\theta, \quad \frac{z_S}{a} = \sqrt{a^2\kappa_0^2 + 2} - \sqrt{a^2\kappa_0^2 + 2\cos(\theta+\alpha)}, \tag{3.3}$$

where θ is the angle between the interface and the wall (see figure 3). For the following, it is important to express the width l_g of the sessile drop base when $\alpha = 0$:

$$\frac{l_g}{a} = 2\int_\pi^{-\pi} \frac{\cos\theta}{\sqrt{a^2\kappa_0^2 + 2\cos\theta}}\,\mathrm{d}\theta = \frac{\pi}{a^3\kappa_0^3} + O\left(a^{-7}\kappa_0^{-7}\right). \tag{3.4}$$

The approximation in the limit of small droplet sizes, i.e. when the drop shape is almost circular with radius κ_0^{-1}, is better understood by noting that the drop weight $\pi\rho g\kappa_0^{-2}$ has to balance the pressure force $l_g\sigma\kappa_0$ applying on the wall. It is accurate to within 7 % for droplet radii smaller than a.

https://doi.org/10.1017/jfm.2013.470 Published online by Cambridge University Press

On the other hand, in the inner region, i.e. that in contact with the air film, the profile of the drop results from a balance between the pressure due to the viscous flow in the air film and capillarity. Assuming a lubrication flow, the pressure in the film evolves according to (Batchelor 1967)

$$p' = -\frac{12\eta}{h^3}\left(q - \frac{Vh}{2}\right), \tag{3.5}$$

where the prime denotes the derivative with respect to x, and h and q respectively stand for the thickness of the air film and the air flow rate per unit of width in the film. Using the linearized form of the curvature $\kappa \simeq h''$, (3.2) and (3.5) combine into

$$a^2 h''' + \cos\alpha\, h' + \sin\alpha = 6a^2 Ca \frac{2q/V - h}{h^3}. \tag{3.6}$$

For the experimental conditions, $Ca \sim 10^{-3}$ and $\sin\alpha \ll Ca(a/h)^2 \sim 10^2$ (which is consistent with the output of the model, see (3.13)). Equation (3.6) can then be approximated by

$$h''' = 6Ca \frac{2q/V - h}{h^3}. \tag{3.7}$$

Introducing the dimensionless film thickness H and coordinate ξ defined as

$$H(\xi) = \frac{h}{h_0} \quad \text{with } \xi = \frac{x}{l_\eta}, \quad l_\eta = \frac{h_0}{(6Ca)^{1/3}}, \quad h_0 = \frac{2q}{V}, \tag{3.8}$$

equation (3.7) adopts the well-known dimensionless form

$$H''' = \frac{1 - H}{H^3}. \tag{3.9}$$

3.1. *Large drops*

As seen in § 2, for 'large' drops the film longitudinal profile exhibits a long and almost flat portion. We call this regime the large-drop regime. It corresponds to the case when the length l_g of the flat area at the bottom of the sessile drop is much larger than the length l_η of the visco-capillary transition region introduced in (3.8).

In the flat portion of the film $H''' \simeq 0$. One may thus write $H = 1 + \epsilon$ with $\epsilon \ll 1$ and obtain

$$\epsilon = A\mathrm{e}^{-\xi} + B\cos\left(\frac{\sqrt{3}}{2}\xi + \phi\right)\mathrm{e}^{\xi/2}, \tag{3.10}$$

after linearizing and solving (3.9). As the length of the flat region separating the upstream from the downstream side of the drop can theoretically be made arbitrarily long, asymptotic expressions for each of them can be sought separately, in the same manner as in Bretherton (1961). Note that this length can however be limited for stability reasons, as direct observations on large drops suggest. For the upstream portion, i.e. as $\xi \to -\infty$, (3.9) has to be solved with the asymptotic boundary conditions

$$H(+\infty) = 1, \quad H'(+\infty) = 0. \tag{3.11}$$

Using (3.10), with the arbitrary constant $A = 1$, and with $B = 0$ corresponding to those boundary conditions, numerical integration of (3.9) from $\xi = 20 \gg 1$ yields the

https://doi.org/10.1017/jfm.2013.470 Published online by Cambridge University Press

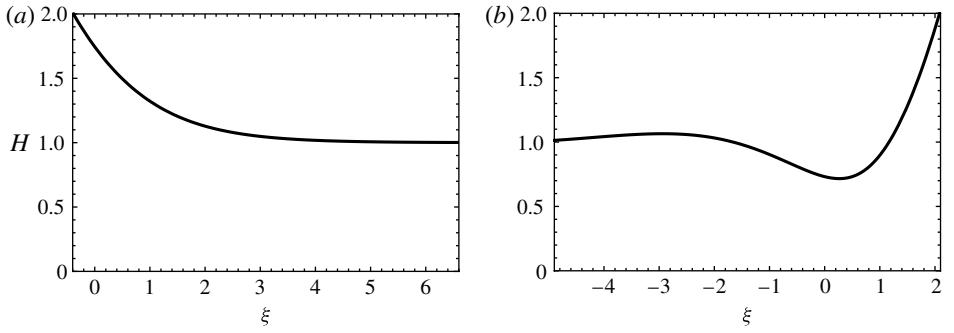


FIGURE 4. Dimensionless upstream (a) and downstream (b) profiles of the air film thickness for a large drop.

asymptotic behaviour $H''(\xi) \simeq 0.643$ as $\xi \to -\infty$, as already found by Bretherton (1961).

For the downstream portion, i.e. as $\xi \to +\infty$, (3.9) has to be solved with the asymptotic boundary conditions

$$H(-\infty) = 1, \quad H'(-\infty) = 0, \quad H''(+\infty) \simeq 0.643, \tag{3.12}$$

since, at the bottom of the drop, the same curvature has to be recovered as for the upstream side of the drop. This is valid for the case $\alpha = 0$. Equation (3.10) is now used with $A = 0$ and the arbitrary constant $\phi = 0$. B is determined by a shooting method, so as to match the boundary conditions (3.12). This yields $B \simeq 0.321$ and a master shape exhibiting a minimum $H_{min} \simeq 0.716$ and a first local maximum $H_{max} \simeq 1.065$ as shown on figure 4.

By matching the asymptotic constant curvature $H''(+\infty)$ of boundary condition (3.12) with the actual curvature $h'' = \kappa_b$ at the bottom of the sessile drop (see figure 3), one obtains the air film thickness h_0 in the flat portion under the drop as

$$h_0 \simeq 2.123\, Ca^{2/3} \kappa_b^{-1}. \tag{3.13}$$

Note that κ_b is related to κ_0 through the shape of the sessile drop: for a 2D drop, (3.3) yields $\kappa_b = \sqrt{\kappa_0^2 + 2/a^2}$. In the asymptotic regime, the dimple in the air film, on the downstream profile, can be characterized by the minimal thickness $h_{min} \simeq 0.716\, h_0$, the first local maximal thickness $h_{max} \simeq 1.065\, h_0$ and the horizontal spacing $\lambda \simeq 4.238\, Ca^{1/3} \kappa_b^{-1}$ between them. Note also that, in the case $\alpha > 0$, the downstream profile would only be slightly modified, because the drop curvature κ_b would be smaller than that of the upstream side of the drop, but this would hardly modify h_0, as, for small Ca, $h'' = 0$ in (3.6) yields

$$\frac{h}{h_0} \simeq 1 - \frac{\sin\alpha}{0.643^2 (a\kappa_b)^2} (6Ca)^{1/3} \simeq 1 - 0.751 \frac{\sin\alpha}{(a\kappa_b)^2} Ca^{1/3}, \tag{3.14}$$

which is very close to 1 for the present experimental conditions.

Let us finally make two crucial remarks. First, although no global balance has been written, the weight of the drop is exactly balanced by the lubrication pressure in the air film. This is a consequence of (3.2) which equilibrates the lubrication and capillary pressures with the hydrostatic pressure. Second, the drop weight is sustained because the resultant of the pressure projected along $\boldsymbol{e}_z$ is positive. This is possible only when the air film thickness profile is asymmetric along $\boldsymbol{e}_x$ (a symmetric profile would give

https://doi.org/10.1017/jfm.2013.470 Published online by Cambridge University Press

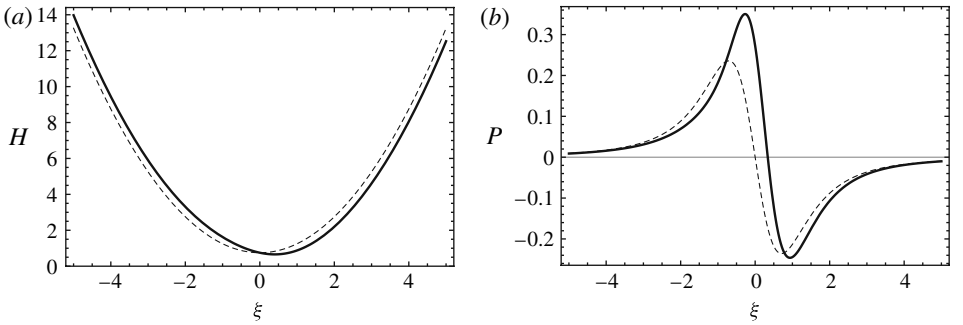


FIGURE 5. Dimensionless air film thickness (a) and pressure in the film (b) for a 'small' drop (plotted for $K = 1$). The dashed and solid lines respectively correspond to the undeformed parabolic profile H_0 and the deformed profile $H_0 + \epsilon$.

an odd pressure profile whose integral would vanish), or when lubrication breaks down, as for bearings where cavitation breaks the anti-symmetry of the pressure profile (Dowson & Taylor 1979). In the present case, the asymmetry of the film results from the deformation of the drop which is itself a consequence of the lubrication pressure field. This coupling will appear even more clearly in the treatment of small drops to which we turn now.

3.2. *Small drops*

For 'small' drops, the shape of the air film is radically different. The upstream and downstream visco-capillary regions merge, and the drop adopts an almost circular shape while the air film profile become close to parabolic. This corresponds to the case when $l_g < l_\eta$. One therefore naturally seeks a film thickness that is a perturbation of a parabolic profile $H_0(\xi)$, with an *a priori* unknown dimensionless curvature K, corresponding to an undeformed drop, i.e.

$$H = H_0 + \epsilon = C + K\frac{\xi^2}{2} + \epsilon, \tag{3.15}$$

where C is an unknown constant and the perturbation ϵ satisfies $\epsilon \ll H_0$, as will be checked *a posteriori*. Equation (3.9) then becomes

$$\epsilon''' = \frac{1 - H_0}{H_0^3} + O(\epsilon), \tag{3.16}$$

which has a single real solution

$$\epsilon = -\left(\frac{2}{3K}\right)^{3/2} \arctan\left(\sqrt{\frac{2K}{3}}\xi\right) \quad \text{for } C = \frac{3}{4}. \tag{3.17}$$

This solution is plotted in figure 5 for $K = 1$.

In order to determine both K and h_0, two matching conditions have now to be found. The first one is the matching of the curvatures $H''(\pm\infty)$ with κ_b, as in § 3.1. The only other relevant matching possibility is global: the resultant of the pressure has to balance the drop weight (note that this was automatically satisfied in § 3.1 by connecting a flat film portion with one having a uniform curvature κ_b). One therefore needs to determine the pressure field in the air film. This field can be thought of

https://doi.org/10.1017/jfm.2013.470 Published online by Cambridge University Press

as the sum of an odd contribution P_0, resulting from the parabolic shape H_0, which is modulated by a small symmetric contribution P_1, resulting from the small odd deformation ϵ, i.e.

$$P \simeq P_0 + P_1 = -\int_{-\infty}^{x} \frac{H_0 - 1}{H_0^3}\,\mathrm{d}\xi + P_1 = -\frac{16\xi}{3(3+2K\xi^2)^2} + P_1, \tag{3.18}$$

where the dimensionless Laplace's law $P' = -H'''$ has been used. P_1 is then determined from the first-order term in ϵ in (3.9) with the boundary condition $P_1(\pm\infty) = 0$ yielding

$$P_1 = -\int \frac{2H_0 - 3}{H_0^4}\epsilon\,\mathrm{d}\xi = \frac{2^3}{3^4K^2}\left[\pi^2 - 4\arctan^2\left(\sqrt{\frac{2K}{3}}\xi\right)\right.$$
$$\left. - 24\frac{(8 + 7K\xi^2 + 2K^2\xi^4) + \sqrt{\frac{2K}{3}}\xi(27 + 16K\xi^2 + 4K^2\xi^4)\arctan\left(\sqrt{\frac{2K}{3}}\xi\right)}{(3+2K\xi^2)^3}\right]. \tag{3.19}$$

Since P_0 is odd, it does not contribute to the resultant of the pressure, and the latter, in its dimensionless form, is then

$$\frac{f_z}{\sigma Ca^{1/3}} = F_Z = \int_{-\infty}^{\infty} P_1\cos\theta\,\mathrm{d}\xi \simeq \int_{-\infty}^{\infty} P_1\,\mathrm{d}\xi = \frac{\pi}{9}\left(\frac{2}{3K}\right)^{5/2}. \tag{3.20}$$

Note that (3.20) represents the dominant contribution to the vertical force, since the zero-order term in $\int \tau\sin\theta\,\mathrm{d}x$ is exactly nil, while the first-order term is of order $\sigma Ca^{2/3}K^{-5/2}$, which will be shown to be much smaller than $\sigma Ca^{1/3}F_Z$ for small capillary numbers in (3.21).

Finally, the two matching conditions $\kappa_b = h_0K/l_\eta^2 = (6Ca)^{2/3}K/h_0$, for the interface curvature, and $\pi(a\kappa_0)^{-2}\cos\alpha = 6Ca(l_\eta/h_0)^2F_Z = (6Ca)^{1/3}F_Z$, for the weight of the drop, yield the actual minimal air film thickness

$$h_{min} = \frac{3}{4}h_0 = 2^{-1/5}Ca^{4/5}\left(\frac{a^2\kappa_0^2}{\cos\alpha}\right)^{2/5}\kappa_b^{-1} \simeq 0.871\,Ca^{4/5}\left(\frac{a^2\kappa_0^2}{\cos\alpha}\right)^{2/5}\kappa_b^{-1}. \tag{3.21}$$

3.3. *Air drag*

In the experiment, the position of the drop in the rotating cylinder is determined by the ratio of its weight to the air drag. Beside the body drag due to the main air flow around the drop, the air in the lubrication film flow under the drop generates an additional drag which can be dominant. This latter drag *a priori* has two contributions: one due to the shear stress at the drop interface

$$\int \tau\cos\theta\mathrm{d}x = -\int \eta u_z|_h\cos\theta\,\mathrm{d}x = \sigma(6Ca)^{2/3}\int \frac{3-2H}{6H^2}\cos\theta\,\mathrm{d}\xi, \tag{3.22}$$

https://doi.org/10.1017/jfm.2013.470 Published online by Cambridge University Press

and the other due to the pressure

$$-\int p\sin\theta \mathrm{d}x = -\sigma\int(\kappa_b-\kappa)\sin\theta\,\mathrm{d}x = \sigma(6Ca)^{1/3}\int\int\frac{1-H}{H^3}\sin\theta\,\mathrm{d}\xi\mathrm{d}\xi. \quad (3.23)$$

For large drops, the shear stress by definition applies over a length l_g that is much larger than the typical length l_η and therefore, even for small capillary numbers, both drag terms are important. The pressure term (3.23) in the flat portion of the film vanishes, as $\sin\theta = 0$, the contribution of the upstream and downstream transition regions is numerically estimated from the profiles in figure 4, while the dimensionless drag term is simply $(1/6)l_g/l_\eta$, since $H = 1$ in the flat region. This yields

$$f_x = \sigma\left[1.224(6Ca)^{1/3} + \frac{1}{6}\frac{l_g}{l_\eta}(6Ca)^{2/3}\right] \simeq \sigma\left(2.22 + 0.471 l_g\kappa_b\right)Ca^{1/3}. \quad (3.24)$$

For small drops, on the other hand, the shear stress applies over a typical length l_η and therefore, for small capillary numbers, the pressure term of the air drag is dominant. Using (3.23), with the zero-order pressure field P_0 from (3.18), yields the resultant force tangential to the wall

$$\frac{f_x}{\sigma(6Ca)^{1/3}} = -\int_{-\infty}^{\infty}P_0\sin\theta\,\mathrm{d}\xi = \frac{8K\left[2\sqrt{3}\arccos\sqrt{\dfrac{3K}{2}} - 3\sqrt{(2-3K)K}\right]}{9\left[(2-3K)K\right]^{3/2}}$$
$$= \frac{8}{9K} + O(K^{-2}), \quad (3.25)$$

which can also be expressed as

$$f_x = 2^{11/5}\sigma Ca^{1/5}\left(\frac{a^2\kappa_0^2}{\cos\alpha}\right)^{-2/5} \simeq 4.594\sigma Ca^{1/5}\left(\frac{a^2\kappa_0^2}{\cos\alpha}\right)^{-2/5}. \quad (3.26)$$

3.4. *Numerical integration*

Parallel to the asymptotic approach used in §§ 3.1–3.3, we also numerically integrated the nonlinear form of (3.6), i.e.

$$\partial_{ss}\theta + \frac{\sin(\theta+\alpha)}{a^2} + 6Ca\cos\theta\frac{h-2q}{h^3} = 0, \quad \partial_s h = \sin\theta, \quad \partial_s x = \cos\theta, \quad (3.27)$$

where s stands for the curvilinear coordinates along the drop interface profile, with the following initial conditions:

$$\theta(0) = -\pi/2, \quad \partial_s\theta(0) = \kappa_0, \quad h(0) = z_S(-\pi/2) + \Delta h, \quad x(0) = x_S(-\pi/2). \quad (3.28)$$

A shooting method was then used, with the *a priori* unknown flow rate q and vertical shift of the drop Δh (with respect to the sessile configuration) as adjustable parameters, so as to match the initial slope, curvature and sessile drop width in $\theta = \pi/2$.

This approach permits the study of configurations where the capillary number is not small. We use it here to illustrate the cross-over between the large- and the small-drop regimes that we discussed previously, and also for the case when $\alpha \neq 0$. Figure 6 shows three numerical profiles for three different drop sizes. These profiles illustrate the formation and the evolution of a plateau in the air film thickness as the drop size increases.

https://doi.org/10.1017/jfm.2013.470 Published online by Cambridge University Press

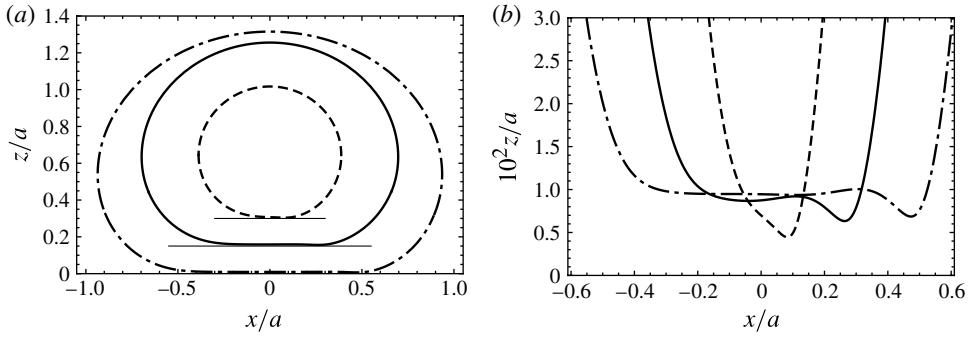


FIGURE 6. Drop shapes (*a*) and air film thicknesses (*b*) obtained by numerical integration of (3.27). $Ca = 10^{-3}$, the wall is horizontal ($\alpha = 0$), and the curvatures at the equator are $a\kappa_0 = 2.5$ (dashed line), 1.4 (solid line) and 0.9 (dashed-dotted line). The first and second profiles in (*a*) are vertically shifted by 0.3 and 0.15, respectively.

Drop	V (m s^{-1})	D (mm)	α (deg.)	h (μm)	$10^3 Ca$ (—)	a (mm)	l_g/l_η (—)	κ_b^{-1} (mm)	h_0 (μm)	α_{eq} (deg.)
1	1.43	1.10	40.5	4.8	1.24	1.49	1.85	0.250	6.3	53.9
2	1.65	2.32	13.5	4.0	1.44	1.49	2.90	0.425	11.5	8.6
3	1.43	2.77	3.3	5.0	1.24	1.49	3.22	0.467	11.5	11.6

TABLE 1. Experimental parameters and predictions corresponding to the three profiles shown in figure 7. $a = 1.49$ mm. κ_b is computed from D and a, assuming a 3D axi-symmetric drop. h_0 is computed from (3.13) corresponding to the large drop limit. The equivalent inclination angle is $\alpha_{eq} = \arcsin(f_x/f_z)$.

4. Comparison

We now turn to the comparison of the predictions of § 3 with the air film thickness we measured. In order to compare the 3D shape of the air film with the predictions of the 2D model, we focus on the profile in the plane of symmetry of the drop, i.e. parallel to the direction $\boldsymbol{e_x}$ of the wall motion. As we will see, it contains all the important characteristics of the air film necessary to explain the levitation of a drop.

Figure 7 shows three air film thickness profiles, for different drop sizes with similar wall velocities. The parameters of the experiments are listed in table 1. As already mentioned in § 2, the air films are typically a few micrometres thick. Their shapes however strongly depend on the drop size, as predicted in § 3. For the smallest drop, with apparent diameter $D = 1.10$ mm $= 0.74a$ (figure 7*a*), the thickness decreases almost continuously with x, until a minimal value is reached at the upstream side of the air film. The plateau predicted for large drops is barely observed, around $x \simeq 0.4$ mm. This is fully consistent with our model: here $l_g/l_\eta = 1.85$ is comparable to 1, and therefore the visco-capillary transition regions cover most of the drop base. As the drop diameter is increased (figure 7*b,c*), a plateau appears in the film thickness profile. It separates the two transition regions which exhibit shapes similar to those predicted in § 3.1: the upstream profile is monotonic, while the downstream profile oscillates and shows a marked minimum just at the end of the drop base.

https://doi.org/10.1017/jfm.2013.470 Published online by Cambridge University Press

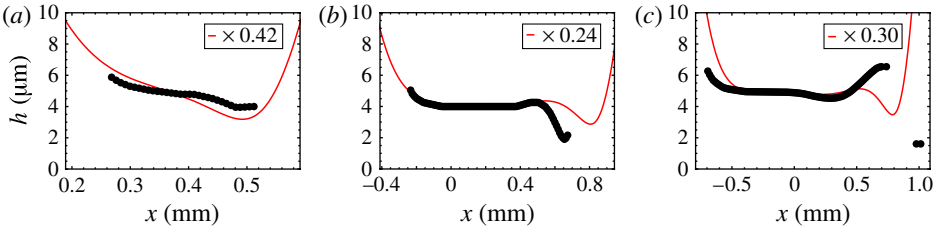


FIGURE 7. Comparison of the experimental profiles of the air film, measured in the plane of symmetry (black circles), with the numerical two-dimensional profiles (red lines) computed with gravity tilted by α: (*a*) corresponds to drop 1, (*b*) drop 2 and (*c*) drop 3, whose parameters are listed in table 1. The thicknesses from the numerical profiles are respectively multiplied by 0.42, 0.24 and 0.30 to show the similarities in the shapes.

The fact that both the general shape and the main characteristics of the air film are correctly captured by the 2D model should not hide that, although the absolute thicknesses are of the same order as in the experiments, they still differ by a substantial factor: the experimental thickness is systematically smaller than that from the model, whether one considers the analytical results, in table 1 (factors of 1.3–2.9 when considering the curvature κ_b of a 3D drop with apparent diameter D), or the numerical integration, in figure 7 (factors 2.4–4.2, as κ_b corresponds to a 2D drop with the same D).

One might think that this difference is a consequence of the assumptions about the flow in the air film: due to the motion in the liquids, the velocity in the air film is not exactly V at the liquid layer surface, nor exactly zero at the drop interface, as we assumed in the model. This results in a slightly smaller lift force than predicted for the same film thickness, i.e. a smaller thickness to levitate the drop. This could explain why a low-viscosity drop is more difficult to levitate: it has a comparatively thinner air film underneath. However, as already stated in § 2, for the fairly high liquid viscosity we used, we could experimentally check that the no-slip condition is a very good approximation. Moreover, an estimation of the boundary layers in the air and in the liquid shows that the velocity difference V between the drop and the wall is essentially achieved across the air film (see the Appendix), as assumed in the model. Similarly, the compressibility of the air in the film, which we neglected in the model, cannot explain the difference. The typical value of the lubrication pressure below the drop is $\eta VD/h_0^2 \sim 10^3$–10^4 Pa which is indeed negligible compared to the 10^5 Pa of the atmospheric pressure (the ratio of order 10^{-2}–10^{-1} is the bearing number used in tribology (Witelski 1998)).

We therefore conclude that the discrepancy is essentially due to the difference between the 2D and 3D configurations. In the former configuration the air flow rate is conserved along x, while in the latter some of the air which is dragged under the drop escapes from the sides resulting in a smaller value of h_0 necessary to built up the same lubrication pressure. This could explain the factors of order unity reported in table 1. We however think that, although the pre-factors are different for the real 3D drops, the scaling laws in (3.13) and (3.21) are still valid and provide important predictions for the film thickness and air drag due to the lubrication flow.

It is also important to realize that any model assuming lubrication theory in the air film, including ours, should not be able, alone, to account for the existence of a velocity threshold for the levitation of a drop. As (3.13) and (3.21) show, for smaller

https://doi.org/10.1017/jfm.2013.470 Published online by Cambridge University Press

and smaller capillary numbers, the film thickness is simply expected to decrease (while the accuracy of the model keeps increasing). We therefore think that the velocity threshold observed in the experiment is due to the existence of a minimum in the air film thickness that one can in practice sustain in the presence of noise and wall roughness, rather than a strict minimum dictated by considerations on a smooth geometry. This is consistent with the facilitated levitation observed over a liquid surface.

5. Conclusion and extension

The levitation of a drop over a moving surface has been studied using a simple and original setup, a rotating cylinder, to achieve a steady state in which the drop is free to move. We observed that the levitation was possible for different drop sizes above a critical surface velocity that increased with drop size. The levitation was experimentally facilitated by covering the cylinder surface with a thin liquid layer and by using a liquid with intermediate viscosity $\nu \sim 50$ cSt. Both smaller and larger viscosities resulted in lower stability and levitation time of the drop. Interferometric measurements yielded the shape and the absolute thickness of the air film dragged underneath the drop by the moving surface.

This film presents a flat region, extending further with increasing drop size, surrounded by a ridge of minimal thickness of the air film, on the downstream and lateral sides. As we showed with a simplified 2D model, this shape is a consequence of the deformation of the drop interface by the pressure due to lubrication flow in the air film. The pressure built-up is responsible for the lift force and explains the levitation of the drop. The 2D model also provides predictions for the air film shape, its absolute thickness and the air drag due to the lubrication flow under the drop, for two asymptotic regimes whose scalings are expected to be valid in the real 3D configuration: large drops, when the bottom of the drop is essentially flat, and small drops, when it is almost spherical.

Let us conclude by mentioning some further investigations of levitating drops that arise naturally from the present study. Measurements of the film thickness and air drag need to be extended to check the validity of the asymptotic predictions we proposed. The precise influence of the liquid viscosity is still not known, nor is the criterion for the practical velocity threshold for levitation. Finally, the steady wake of the drop and the interaction between levitating drops would also worth studying. The experimental system we proposed provides an ideal configuration for those investigations.

Acknowledgement

We warmly thank D. Lohse for the wonderful environment and the setup for conducting this research.

Appendix. Flow in the liquid layer covering the wall

The boundary layer which develops in the liquid layer covering the cylinder inner surface, as the drop passes, is of order

$$\delta \sim \sqrt{\nu D/V} \sim 200\ \mu\text{m}, \tag{A 1}$$

which is smaller than the liquid layer thickness. The equality of the shear stresses at the surface of the liquid layer then relates the velocity variations Δu_{liq}, across the

https://doi.org/10.1017/jfm.2013.470 Published online by Cambridge University Press

boundary layer, and Δu, across the air film, via

$$\eta \Delta u / h_0 \sim \eta_{liq} \Delta u_{liq} / \delta. \tag{A 2}$$

Therefore

$$\frac{\Delta u}{\Delta u_{liq}} \sim \frac{\eta_{liq} h_0}{\eta \delta} \gtrsim 10, \tag{A 3}$$

which means that the velocity difference V between the drop and the wall is essentially achieved across the air film, as assumed in the model.

References

Aussillous, P & Quéré, D. 2001 Liquid marbles. *Nature* **411** (6840), 924–927.

Batchelor, G. K. 1967 *An Introduction to Fluid Dynamics*. Cambridge University Press.

Bluemink, J. J., Lohse, D., Prosperetti, A. & van Wijngaarden, L. 2008 A sphere in a uniformly rotating or shearing flow. *J. Fluid Mech.* **600**, 201–233.

Bluemink, J. J., Lohse, D., Prosperetti, A. & van Wijngaarden, L. 2009 Drag and lift forces on particles in a rotating flow. *J. Fluid Mech.* **643**, 1–31.

Bluemink, J. J., van Nierop, E. A., Luther, S., Deen, N. G., Magnaudet, J., Prosperetti, A. & Lohse, D. 2005 Asymmetry-induced particle drift in a rotating flow. *Phys. Fluids* **17** (7), 072106.

Bretherton, F. P. 1961 The motion of long bubbles in tubes. *J. Fluid Mech.* **10**, 166–188.

Couder, Y., Fort, E., Gautier, C. H. & Boudaoud, A. 2005 From bouncing to floating: noncoalescence of drops on a fluid bath. *Phys. Rev. Lett.* **94** (17) 177801-(4).

Dell'Aversana, P., Banavar, J. R. & Koplik, J. 1996 Suppression of coalescence by shear and temperature gradients. *Phys. Fluids* **8**, 15–28.

Dowson, D & Taylor, C. M. 1979 Cavitation in bearings. *Annu. Rev. Fluid Mech.* **11**, 35–65.

Duchesne, A., Savaro, C., Lebon, L., Pirat, C. & Limat, L. 2013 Multiple rotations of a drop rolling inside a horizontal circular hydraulic jump. *Eur. Phys. Lett.* **102** (6), 64001.

Landau, L. & Levich, B. 1942 Dragging of a liquid by a moving plate. *Acta Physicochim. USSR* **17**, 42–54.

Neitzel, G. P. & Dell'Aversana, P. 2002 Noncoalescence and nonwetting behaviour of liquids. *Annu. Rev. Fluid Mech.* **34**, 267–289.

Pirat, C., Lebon, L., Fruleux, A., Roche, J. -S. & Limat, L. 2010 Gyroscopic instability of a drop trapped inside an inclined circular hydraulic jump. *Phys. Rev. Lett.* **105** (8), 084503.

Quéré, D. 2013 Leidenfrost dynamics. *Annu. Rev. Fluid Mech.* **45**, 197–215.

Smith, M. K. & Neitzel, G. P. 2006 Multiscale modelling in the numerical computation of isothermal non-wetting. *J. Fluid Mech.* **554**, 67–83.

Sreenivas, K. R., De, P. K. & Arakeri, J. H. 1999 Levitation of a drop over a film flow. *J. Fluid Mech.* **380**, 297–307.

Tagawa, Y., van der Molen, J., van Wijngaarden, L. & Sun, C. 2013 Wall forces on a sphere in a rotating liquid-filled cylinder. *Phys. Fluids* **25** (6), 063302.

Tran, T., de Maleprade, H., Sun, C. & Lohse, D. 2013 Air entrainment during impact of droplets on liquid surfaces. *J. Fluid Mech.* **726**, R3.

Tran, T., Staat, H., Prosperetti, A., Sun, C. & Lohse, D. 2012 Drop Impact on Superheated Surfaces. *Phys. Rev. Lett.* **108** (3), 036101.

van der Veen, R. C. A., Tran, T., Lohse, D. & Sun, C. 2012 Direct measurements of air layer profiles under impacting droplets using high-speed colour interferometry. *Phys. Rev.* E **85** (2), 026315.

Witelski, T. P. 1998 Dynamics of air bearing sliders. *Phys. Fluids* **10** (3), 698–708.

https://doi.org/10.1017/jfm.2013.470 Published online by Cambridge University Press